

## MN LUP: X-RAYS FROM A WEAKLY ACCRETING T TAURI STAR

H. M. GÜNTHER

Harvard-Smithsonian Center for Astrophysics, 60 Garden Street, Cambridge, MA 02138, USA

AND

U. WOLTER, J. ROBRADÉ

Universität Hamburg, Hamburger Sternwarte 112, 21029 Hamburg, Germany

AND

S. J. WOLK

Harvard-Smithsonian Center for Astrophysics, 60 Garden Street, Cambridge, MA 02138, USA

*Draft version April 20, 2022*

### ABSTRACT

Young T Tauri stars (TTS) are surrounded by an accretion disk, which over time disperses due to photoevaporation, accretion, and possibly planet formation. The accretion shock on the central star produces an UV/optical veiling continuum, line emission, and X-ray signatures. As the accretion rate decreases, the impact on the central star must change. In this article we study MN Lup, a young star where no indications of a disk are seen in IR observations. We present *XMM-Newton* and *VLT/UVES* observations, some of them taken simultaneously. The X-ray data show that MN Lup is an active star with  $L_X/L_{bol}$  close to the saturation limit. However, we find high densities ( $n_e > 3 \times 10^{10} \text{ cm}^{-3}$ ) in the X-ray grating spectrum. This can be well fitted using an accretion shock model with an accretion rate of  $2 \times 10^{-11} M_\odot \text{ yr}^{-1}$ . Despite the simple  $H\alpha$  line profile which has a broad component, but no absorption signatures as typically seen on accreting TTS, we find rotational modulation in Ca II K and in photospheric absorption lines. In the  $H\alpha$  line we see a prominence in absorption about  $2R_*$  above the stellar surface - the first of its kind on a TTS. MN Lup is also the only TTS where accretion is seen, but no dust disk is detected that could fuel it. We suggest that MN Lup presents a unique and short-lived state in the disk evolution. It may have lost its dust disk only recently and is now accreting the remaining gas at a very low rate.

*Subject headings:* circumstellar matter – Stars: formation – Stars: pre-main sequence – X-rays: stars

### 1. INTRODUCTION

T Tauri stars (TTS) are pre-main sequence stars of spectral type M to F surrounded by a circumstellar disk. They come in two flavors, the classical T Tauri stars (CTTS), which actively accrete from their disk, and the more evolved weak-lined T Tauri stars (WTTS) whose accretion has already stopped. The disks are typically detected in the IR, e.g. in *Spitzer* surveys where they show up as excess emission above the stellar photosphere. To distinguish between CTTS and WTTS, the combination of strong  $H\alpha$  emission and line asymmetry can be used because these are reliable accretion indicators (Muzerolle et al. 1998, 2003). However, there are some exceptions where a low  $H\alpha$  equivalent width (EW) seems to correspond to high mass accretion rates (Littlefair et al. 2004); furthermore, the strength of the intrinsic  $H\alpha$  line also depends on the spectral type and on the chromospheric activity of the specific star. In extreme cases, the chromosphere alone can produce  $H\alpha$  in emission with an EW of a few Å.

Several pathways are possible to evolve an accreting CTTS to a non-accreting WTTS through disk evolution. Espaillat et al. (2012) differentiate between “pre-transitional disks”, where a gap in the dust disk is opened at some radius and “transitional disks” (Strom et al. 1989) where the innermost 10-50 AU are entirely cleared of micron sized dust grains. Gaps in disks are particu-

larly interesting, since they indicate planet formation – a planet located in the disk would clear its surroundings (Goldreich & Tremaine 1980; Rice et al. 2003; Quillen et al. 2004) and interrupt the mass accretion. Still, some dust often remains inside of the inner disk wall (Espaillat et al. 2010). Sufficiently close-in planets could also be responsible for an inner hole, but other effects, such as photo-evaporation (Clarke et al. 2001; Gorti & Hollenbach 2009; Owen et al. 2012) or the magneto-rotational instability (MRI) (Chiang & Murray-Clay 2007), can cause an inside-out clearing as well.

All TTS have been known for a long time to be copious X-ray emitters (see reviews by Feigelson & Montmerle 1999; Günther 2012). Particularly, they exhibit high levels of coronal activity and stellar flares. Interferometric observations and modeling of the spectral energy distributions reveal that even in CTTS the accretion disk does not reach down to the star, but is truncated at a few stellar radii by the stellar magnetic field. X-ray and FUV radiation ionize the material at the inner disk rim. Thus, the accreting matter follows the magnetic field lines and impacts onto the stellar surface with a velocity close to free-fall (Koenigl 1991; Shu et al. 1994). For a dipolar field the impact would be at high stellar latitude, but modern simulations explore more complicated geometries (e.g. Long et al. 2012).

The kinetic energy of the infalling matter is released in a standing shock wave, which heats the gas to temperatures of the order of 2-3 MK. This accretion hot spot

explains, among other things, the optical veiling of TTS (Calvet & Gullbring 1998).

With sufficiently high quality X-ray data CTTS can be singled out from other X-ray sources by, first, their strong soft X-ray excess (Robrade & Schmitt 2007; Güdel & Telleschi 2007; Günther 2011) and, second, by unusually high densities in the He-like triplets first seen in the CTTS TW Hya (Kastner et al. 2002). These densities were confirmed later in several consecutively deeper observations (Stelzer & Schmitt 2004; Raassen 2009; Brickhouse et al. 2010). High densities in the X-ray emitting regions have been found in a number of CTTS since: BP Tau (Schmitt et al. 2005), V4046 Sgr (Günther et al. 2006; Argiroffi et al. 2012a), RU Lup (Robrade & Schmitt 2007), MP Mus (Argiroffi et al. 2007), Hen 3-600 (Huenemoerder et al. 2007), and V2129 Oph (Argiroffi et al. 2011). However, T Tau itself, although known for its high accretion rate, is an exception to this rule (Güdel et al. 2007). The high densities observed in the He-like triplets can be naturally linked to accretion. The same model nicely explains the observed soft excess and allows us to reconstruct the density and velocity of the infalling material from X-ray emission lines (Günther et al. 2007). Studies in different wavelength regions regularly indicate very different sizes for the accretion spot (Günther et al. 2007; Curran et al. 2011). The reason is unclear, but one explanation would be an inhomogeneous accretion spot, where only parts reach the temperatures of X-ray emitting gas; another possibility would be that the accretion powers an enhanced chromosphere and corona, that emits locally around the accretion shock (Brickhouse et al. 2010; Petrov et al. 2011). Also, the models often assume optically thin emission regions. This depends critically on the dimensions and shape of the accretion spot, but we do not know if the accretion is concentrated in a large, single spot or more widely distributed.

We observed the TTS MN Lup simultaneously with *XMM-Newton* and the *VLT*. In this paper, we concentrate on the results of the X-ray observations. In Sect. 2 we summarize the stellar properties of MN Lup, Sect. 3 contains the details of the observations and the data reduction. Sect. 4 gives the results and Sect. 5 a short discussion. We end with a summary (Sect. 6).

## 2. STELLAR PROPERTIES OF MN LUP

MN Lup was discovered in an X-ray survey of the Lupus star forming region located at a distance of about 150 pc (Krautter et al. 1997). Table 1 shows the stellar parameters.

MN Lup is a pre-main sequence star as evidenced by its Li abundance. *VLT/UVES* Doppler imaging over more than two rotations reveals structures which Strassmeier et al. (2005) interpret as hot spots at high stellar latitude – exactly where they are expected according to the magnetically funneled accretion theory. Very close to them patches of lower intensity are seen. Strassmeier et al. (2005) interpret this as partially shadowed stellar photosphere. The H $\alpha$  EW is  $6.73 \pm 0.52$  Å, higher than in quiescent main-sequence M0 stars (Riaz et al. 2006), but lower than in accreting CTTS, indicating some stellar activity or a low accretion rate. The intermediate inclination angle ensures that MN Lup is not obscured by its disk.

TABLE 1  
STELLAR PARAMETERS FROM STRASSMEIER  
ET AL. (2005)

parameter	symbol	value
distance	$d$	150 pc
spectral type		M0
luminosity	$L_*$	$0.15 \pm 0.03 L_\odot$
radius	$R_*$	$0.90 \pm 0.02 R_\odot$
mass <sup>a</sup>	$M_*$	$0.68^{+0.06}_{-0.10} M_\odot$
mass <sup>b</sup>	$M_*$	$0.54 \pm 0.12 M_\odot$
age		$20 \pm 10$ Myr
period	$P$	$0.439 \pm 0.005$ days
$v \sin i$		$74.6 \pm 1$ km s <sup>-1</sup>
inclination	$i$	$40 - 50^\circ$

<sup>a</sup>evolutionary tracks by Baraffe et al. (1998)

<sup>b</sup>evolutionary tracks by Siess et al. (2000)

TABLE 2  
LOG OF *XMM-Newton* OBSERVATIONS

ObsID	duration	date	OM
0655760101	27 ks	2010-08-03	UVW1
0670580101	39 ks	2011-08-12	UVW1
0670580201	43 ks	2011-08-12	UV grism

Wichmann et al. (1997) derive an optical reddening of  $A_V = 1.11$ . However, in CTTS the veiling changes the intrinsic colors. Gullbring et al. (1998) therefore suggest to use the  $V - R$  color, which is less affected. With this method Strassmeier et al. (2005) derive  $A_V = 0.78$ . Based on the higher extinction and a lower distance to MN Lup of only 140 pc Krautter et al. (1997) derive an X-ray luminosity of  $L_X = 8.6 \times 10^{29}$  erg s<sup>-1</sup> from *ROSAT* observations.

MN Lup has been observed with *Spitzer* in the c2d survey (Padgett et al. 2006) using the IRAC (3.6-8.0 $\mu$ m) and MIPS (24 $\mu$ m, no detection at 70 $\mu$ m) instruments. No IR excess above a stellar photosphere, which would indicate the presence of a dusty disk, was found down to a limit of a fractional disk luminosity  $L_d/L_* < 9.1 \times 10^{-4}$ , significantly lower than for the debris disk of  $\beta$  Pic with  $L_d/L_* = 2 \times 10^{-3}$  (Wahhaj et al. 2010). The c2d survey is sensitive to the dust in disks from a few tenths of an AU out to a few tens of AU.

## 3. OBSERVATIONS AND DATA REDUCTION

MN Lup was observed three times with the X-ray satellite *XMM-Newton*, which provides simultaneous data from the three imaging cameras PN, MOS1 and MOS2 and two reflection grating spectrometers (RGS1 and RGS2). In addition, there is an optical monitor (OM), which provides photometry or grism spectroscopy in the UV to optical range. In 2010 we performed a relatively short exposure to verify the *ROSAT* count rate and test the spectral shape of the source. In 2011 we obtained observations with *XMM-Newton* mostly simultaneous to optical spectroscopy from *VLT/UVES*. This required splitting the X-ray data in two observations in 2011. In this article we concentrate on the X-ray data. Table 2 summarizes the *XMM-Newton* observations. In all cases we used the medium filter to reduce the contamination with optical light. All observations are processed with the Science Analysis System (SAS), version

11.0.0 (Gabriel et al. 2004). We merged all three EPIC detectors for the lightcurve analysis. In all exposures the extraction regions are small (30'' in the MOS and 15'' in the PN), thus the background is negligible compared to the source signal for lightcurves in the energy range 0.2-5.0 keV. For the spectral analysis we applied standard selection criteria to remove phases of high proton background, which would significantly increase the background for high energies. Specifically, the PN observation in 2010 is contaminated, so we use the MOS1 and MOS2 detectors only for spectral fitting in this exposure. For the exposures in 2011 PN, MOS1 and MOS2 data is fitted simultaneously.

Spectral models are fitted using the *SHERPA* tool (Doe et al. 2007). Line fluxes are modeled by intrinsically narrow Gaussian profiles, which are then convolved with the instrumental response function. In the Ne IX and O VII triplets all three lines are fitted simultaneously and the difference in wavelength is fixed. We allow for an overall adjustment of the wavelength to correct a possible error of the wavelength zero point. In all cases, the fitted wavelength agrees with the theoretical value within the uncertainties. In addition to the lines, we fit a constant to account for instrumental background and source continuum. Because the width of the fit window for each line extends only 0.2 Å on either side of the line center this is a good approximation.

The *VLT/UVES* data (Program ID 087.C-0991(A)) was taken on the nights starting 2011-08-11 (13 exposures) and 2011-08-12 (12 exposures), details on the instrument can be found in Dekker et al. (2000). The exposure time was set to 20 minutes throughout. *UVES* was operated in dichroic mode. The slit width in both *UVES* arms was 0.9'', resulting in a spectral resolution of about 45000. The *UVES* data was reduced using the *ESO* pipeline. The relative timing of the *XMM-Newton* and *VLT/UVES* observations can be seen in Fig. 1.

## 4. RESULTS

### 4.1. Lightcurves

In this section we discuss the lightcurves extracted from the CCD detectors and the OM. In figure 1, time is counted from the beginning of the first observation in each year. The rotation period of MN Lup is  $0.0439 \pm 0.005$  days (Strassmeier et al. 2005). This uncertainty amounts to 10 rotations over one year, which is too large to calculate the relative phase between the observations taken in 2010 and 2011. Thus, the rotational phase is arbitrarily set to 0 at the beginning of the first X-ray observation in each year.

Table 2 shows that the OM operated with the UVW1 filter, which approximately covers the wavelength range 2500-3500 Å in the first two observations and with the UV grism in the last observation. The middle panels in Fig. 1 show the OM lightcurve. In the first two observations, the count rate of MN Lup was read out in a fast window, which provides very high time resolution. However, MN Lup is so bright, that within the fast window little background area is available. Thus, the background subtraction is very sensitive to an accurate positioning of the target. This leads to small changes in the quiescent count rate between individual exposures. During one X-ray observation, the OM performed multiple exposures. Time delay between exposures causes missing points in

the lightcurve, e.g. at 15 and 28 ks in the second observation. The luminosity of MN Lup is comparable to other sources in the field, thus its dispersed grism spectrum is contaminated by the zeroth order of several field stars. Therefore, we extract only the zeroth order of our target MN Lup using simple aperture photometry on the pipeline processed OM images. While the count rate in the zeroth order is not flux calibrated, we should be able to see relative changes in brightness during the observation. The UV grism covers the wavelength range 1800-3500 Å and its count rates are scaled to match the observations with the UVW1 filter at the quiescent level.

The lower panels of Fig. 1 show the X-ray lightcurve. It is divided into two bands from 0.2-0.8 keV and 0.8-5.0 keV. There is little signal above 5 keV and the separation between the two bands is chosen such that their count rates (and thus the signal-to-noise ratio (SNR) in the lightcurves) are comparable. The upper panels in the figure show the H $\alpha$  EW, which is discussed in Sect. 4.7.

The UV lightcurve is mostly flat around 1 count s<sup>-1</sup> with three noticeable flares, all in the second observation around 19, 28 and 36 ks; the corresponding increases in count rate are factors of 5, 2, and 2.5, respectively. Those flares are very short (about 0.5, 1.5 and 1 ks) and all of them are seen in X-rays, most clearly in the hard band. The largest change in X-ray count rate is observed for the last flare, where the count rate doubles. The brightest UV flare, at 19 ks, has only a weak X-ray counterpart. Conversely, the X-ray count rate was much higher in 2010 (first observation) than in the quiescent state in 2011, but the OM count rate is almost the same; the small difference might be due to the difficulties in the background determination in the fast window. Similarly, the X-ray count rate increases in the last observation after about 100 ks by a factor of 2 and shows notable hardening, but no comparable change is seen in the OM.

The hardening of the X-ray emission during the three short flares in the second observation suggests that these are caused by coronal activity as opposed to accretion events. However, it is then surprising that the much longer X-ray activity in the first and third observation has no or only weak UV counterparts. Correlations between X-ray and UV/optical emission in CTTS have been searched for for some time (Gullbring et al. 1997) with little success. In surveys of the ONC (Stassun et al. 2006) and the Taurus molecular cloud (Audard et al. 2007) X-ray and UV/optical lightcurves are uncorrelated with very few exceptions. Both studies conclude, that the X-ray variability is dominated by coronal activity, while the UV shows the rotational modulation of accretion spots. Stassun et al. (2006) find two examples of short (hours) X-ray and optical bursts, that they interpret as “white-light” flares. Flares are observed with a higher time resolution on non-accreting stars, such as CN Leonis (Schmitt et al. 2008) and Proxima Centauri (Fuhrmeister et al. 2011). Both studies used simultaneous *XMM-Newton* and *VLT/UVES* data in a similar setup to our observations of MN Lup and find bright flares (increase in luminosity > 10 in X-ray, UV, and optical) that last less than an hour. The higher luminosity in those observations allows the authors to constrain the physics better and they show that the events are due to coronal and chromospheric activity. The three short bursts in our second observation show a similar pat-

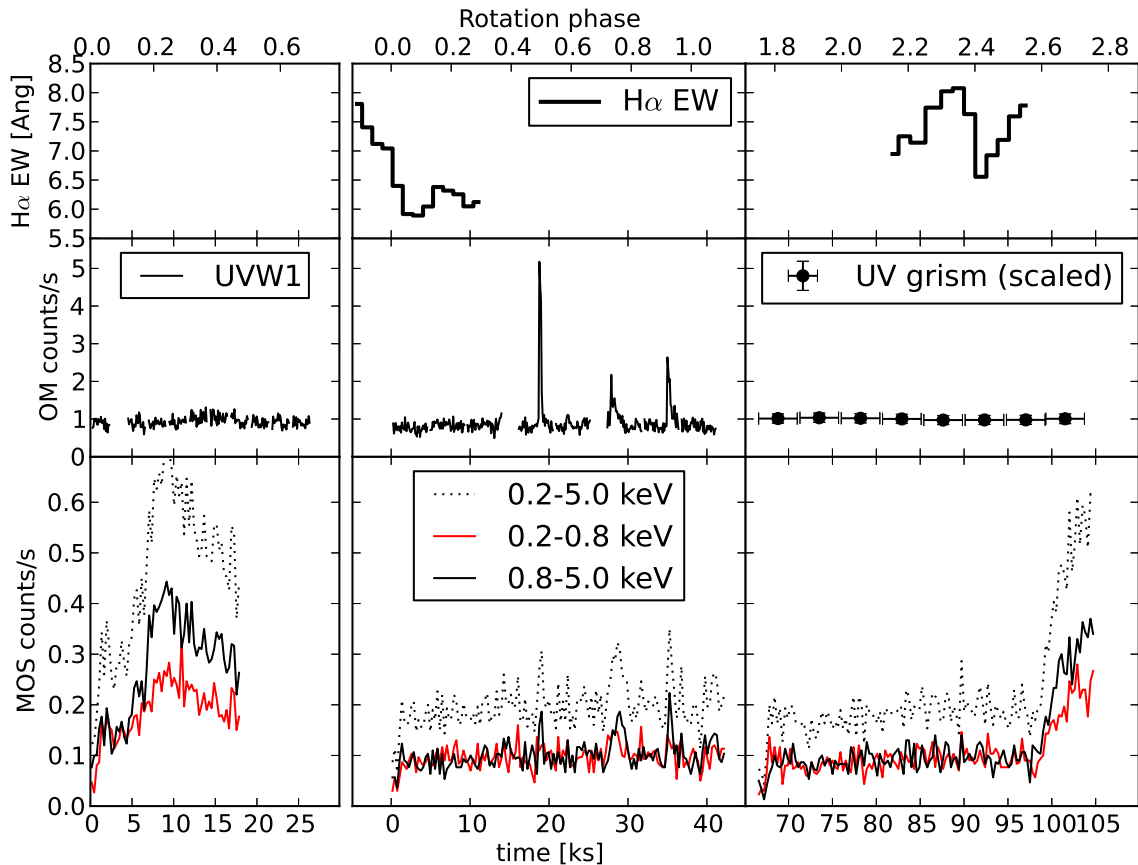


FIG. 1.— Lightcurves from all three *XMM-Newton* observations and  $H\alpha$  EW from *VLT/UVES*. The first X-ray observation is from 2010-08-03, the other two are taken about one year later on 2011-08-12. The time is counted from the beginning of the first X-ray observation in each year. Similarly, the rotational phase is set to 0 at  $t = 0$ . *Top*:  $H\alpha$  EW from the *UVES* data. *Middle*: OM data, binned to 100 s. In the last observation the OM operated with the UV grism, which has a different wavelength range. The rate is scaled to match the quiescent UVW1 count rate. Error bars along the x-axis indicate the exposure time of the grism data. *Bottom*: EPIC count rate, binned to 300 s. In the energy bands shown the background is negligible. See the electronic edition of the Journal for a color version of this figure.

tern and we conclude that we observe three short “white-light” flares on MN Lup.

#### 4.2. CCD spectroscopy

We fit the CCD spectra of all three observations simultaneously. The data are binned to 15 counts per bin. The fit is done with a single absorption component and three optically thin, collisionally dominated emission components (APEC models, Brickhouse et al. 2005). We couple the temperatures of the three components, such that the value of  $T_1$ ,  $T_2$ , and  $T_3$  is the same in each exposure, but allow independent normalizations for 2010, 2011 quiescent phase ( $t < 98$  ks), and 2011 X-ray flare ( $t > 98$  ks) because the lightcurve already shows that MN Lup was significantly brighter in 2010 than in 2011. This model gives a statistically acceptable fit (red.  $\chi^2 = 0.93$ ), but all spectra show systematic residuals at energies where strong emission lines are found in the grating spectrum. Thus, we also fit the abundances of the most important elements (O, Ne, Fe); table 3 gives the best-fit values relative to the solar abundances of Grevesse & Sauval (1998). The addition of the abundances as free parameters, which is *not required* by the  $\chi^2$  value, but motivated from systematics in the residuals and the grating spectrum, leads to a  $\chi^2 \ll 1$  and larger uncertainties on all parameters of the model. The abundances show a trend with the inverse first ionization potential (IFIP effect),

where elements like Ne with a high first ionization potential are more abundant compared with the sun and elements of low FIP like Fe are less abundant. Such an abundance pattern is typical for active stars (see review of Güdel & Nazé 2009).

In CCD spectroscopy there is often an ambiguity between absorption and the amount of cool plasma, such that a higher absorbing column density can be compensated by a larger emission measure with very little changes in the total spectrum; this ambiguity can only be broken with grating spectroscopy of high SNR. Therefore we consider two cases: First, we fix the absorption to  $N_H = 1.4 \times 10^{21} \text{ cm}^{-2}$ , which corresponds to  $A_V = 0.78$  (Strassmeier et al. 2005) using the relation between optical reddening and X-ray column density from Vuong et al. (2003). In the second model we fit the absorption as a free parameter, resulting in  $N_H = (2 \pm 1) \times 10^{20} \text{ cm}^{-2}$  (table 3). Figure 2 displays the model and the PN data from the second observation. The fit values for both models agree within the errors except for the volume emission measure ( $VEM$ ) of the soft component, which is about 25 times larger for the fixed absorbing column density of  $N_H = 1.4 \times 10^{21} \text{ cm}^{-2}$ .

In previous Doppler imaging, large-scale temperature differences are found over the stellar photosphere. These variations are interpreted as absorption by the accretion column (Strassmeier et al. 2005). If this inter-

TABLE 3  
BEST-FIT MODEL PARAMETERS ( $1\sigma$  CONFIDENCE INTERVALS).

parameter	unit	2010	2011	2011
		MOS only	quiescent	flare
$N_H$	$10^{21} \text{ cm}^{-2}$	...	$0.2 \pm 0.1^c$	...
$VEM_1$	$10^{52} \text{ cm}^{-3}$	$2 \pm 1$	$1.3^{+0.7}_{-0.2}$	$1.9^{+1.5}_{-0.7}$
$VEM_2$	$10^{52} \text{ cm}^{-3}$	$3.8 \pm 0.6$	$2.4 \pm 0.3$	$3.1 \pm 0.6$
$VEM_3$	$10^{52} \text{ cm}^{-3}$	$12.5 \pm 0.6$	$2.6 \pm 0.2$	$13.3 \pm 0.9$
$kT_1$	keV	...	$0.14^{+0.02c}_{-0.01}$	...
$kT_2$	keV	...	$0.43^{+0.04c}_{-0.01}$	...
$kT_3$	keV	...	$2.3 \pm 0.2^c$	...
$\log L_X^a$	$\text{erg s}^{-1}$	30.4	30.0	30.4
O	b	...	$0.69^{+0.15c}_{-0.08}$	...
Ne	b	...	$2.2 \pm 0.3^c$	...
Fe	b	...	$0.45 \pm 0.07^c$	...
red. $\chi^2$	0.71 (for simultaneous fit of all 3 datasets)			

<sup>a</sup>unabsorbed flux in the energy range 0.2-5.0 keV

<sup>b</sup>relative to Grevesse & Sauval (1998)

<sup>c</sup>This value is used for all three datasets.

pretation is correct, then the X-ray emission might or might not be subject to the same absorbing column density, depending on the location of the emitting region. If the coronal structures are located close to the pole, then they could be seen through significantly less absorption. X-ray emission from the accretion shock might be partly covered by the accretion funnels, but in this case we would expect significant absorption in the fit. Consequently, the unabsorbed luminosities  $L_X$  differ by factors of a few between the two models. Strassmeier et al. (2005) calculate the bolometric luminosity of MN Lup as  $L_{bol} = 0.14 \pm 0.02 L_\odot$ , which leads to  $\log(L_X/L_{bol}) = -2.3$  or  $-2.7$ , for the high or low value of  $N_H$ , respectively. Cool stars saturate at an activity level of  $\log(L_X/L_{bol}) \approx -3$  (Stauffer et al. 1994; Güdel & Nazé 2009, and references therein). In either case MN Lup is an active star consistent with the IFIP pattern found in the abundances. However, if the model with the higher value for  $N_H$  were correct, then MN Lup would be significantly brighter than the saturation limit and its X-ray flux would be totally dominated by the cool plasma. This would imply high values for the accretion rate, which are incompatible with the H $\alpha$  data (see Sect. 4.7). Thus, we consider the model with  $N_H = 1.4 \times 10^{21} \text{ cm}^{-2}$  unphysical.

Comparing the flare and the quiescent phase in 2011, we see that the volume emission measure in the flare increases significantly. The strongest increase, by a factor of five, happens in the hottest component. This is not unexpected. Given that the temperature  $T_3$  in our model is forced to be the same for all exposures, the extra flare emission must manifest itself as a larger VEM. The VEM in 2010 is comparable to the flare phase in 2011 for all temperature components, which indicates that the observation in 2010 happened in a period of considerable activity as well.

#### 4.3. X-ray grating spectroscopy

Figure 3 shows the merged RGS spectra for the observations in 2011. The signal in the high-resolution grating spectrum is low, thus only few line fluxes can be mea-

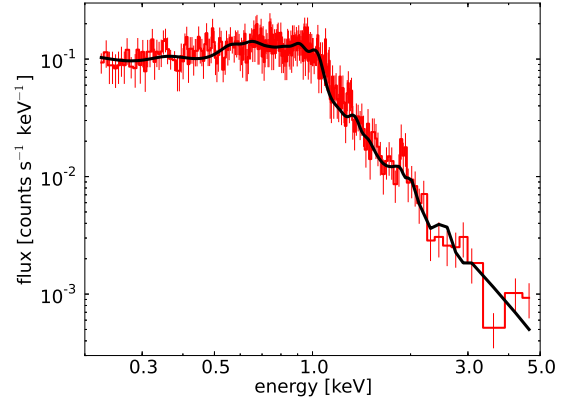


FIG. 2.— PN spectrum from the second observation binned to 15 counts per bin (red/gray). The best fit model with three optically thin, collisionally dominated emission components is overlaid (black). See the electronic edition of the Journal for a color version of this figure.

TABLE 4  
LINE FLUXES ( $1\sigma$  CONFIDENCE INTERVALS).

Line	$\lambda$ [Å]	counts	photon flux [ $\text{s}^{-1} \text{ cm}^{-2}$ ]	luminosity <sup>a</sup> [ $10^{27} \text{ erg s}^{-1}$ ]
RGS1				
O VIII Ly $\alpha$	18.97	38.8	$11.4 \times 10^{-6}$	$37 \pm 9$
O VII r	21.6	16.7	$5.8 \times 10^{-6}$	$17 \pm 7$
O VII i	21.8	11.7	$4.3 \times 10^{-6}$	$13 \pm 6$
O VII f	22.1	8.9	$3.2 \times 10^{-6}$	$10 \pm 6$
RGS2				
Ne X Ly $\alpha$	12.13	14.3	$3.1 \times 10^{-6}$	$14 \pm 9$
Ne IX r	13.45	21.6	$4.6 \times 10^{-6}$	$19 \pm 8$
Ne IX i	13.55	12.0	$2.5 \times 10^{-6}$	$11 \pm 7$
Ne IX f	13.70	21.2	$4.4 \times 10^{-6}$	$19 \pm 9$
Fe XVII	17.05/17.10	20.9	$5.0 \times 10^{-6}$	$18 \pm 11$
O VIII Ly $\alpha$	18.97	39.1	$10.2 \times 10^{-6}$	$33 \pm 10$

<sup>a</sup>corrected for  $N_H = 2.1 \times 10^{20} \text{ cm}^{-2}$

sured. All lines strong enough to fit the line flux are marked and given in table 4. The intrinsic line width is much less than the instrumental broadening and thus can be fixed. From the fitted number of counts and the effective area the intrinsic line luminosity is calculated assuming a distance of 150 pc and the absorbing column density from table 3; the uncertainty of the count number and the uncertainty on  $N_H$  both contribute to the uncertainties on the luminosity given in the table. The detected lines originate from H and He-like neon and oxygen and from Fe XVII. Due to missing chips the wavelength coverage of both RGS is not complete and O VIII 18.97 Å is the only line detected in both detectors. Its flux is compatible in RGS1 and RGS2.

The He-like triplets of Ne IX and O VII are particularly important, because their line ratios are temperature and density-sensitive. These triplets consist of a resonance ( $r$ ), an intercombination ( $i$ ), and a forbidden line ( $f$ ) (Gabriel & Jordan 1969; Porquet et al. 2001). Two ratios ( $R = f/i$  and  $G = (f + i)/r$ ) are defined from the three observed lines. If the emitting plasma has high electron densities  $n_e$  or strong ambient UV photon fields then the  $R$ -ratio falls below its low-density limit, because electrons are collisionally or radiatively excited from the

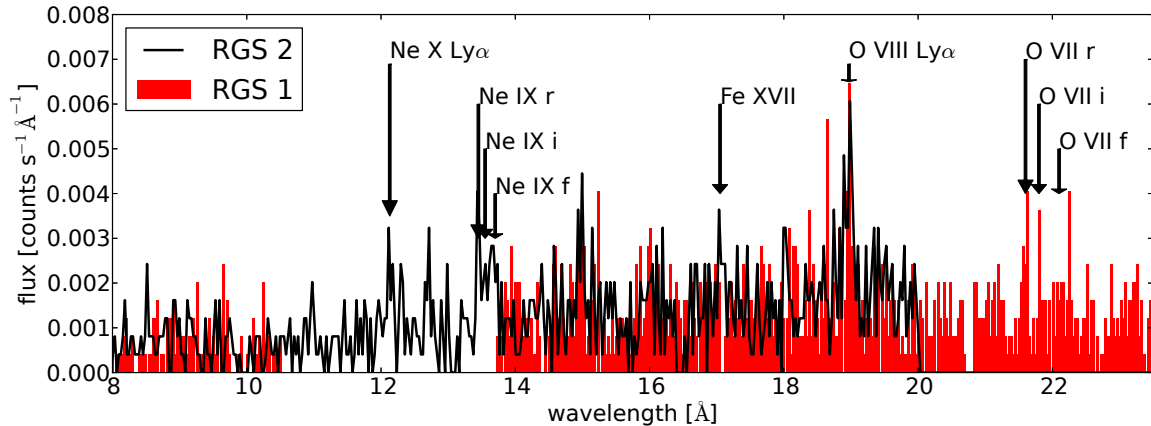


FIG. 3.— RGS spectra of MN Lup. See the electronic edition of the Journal for a color version of this figure.

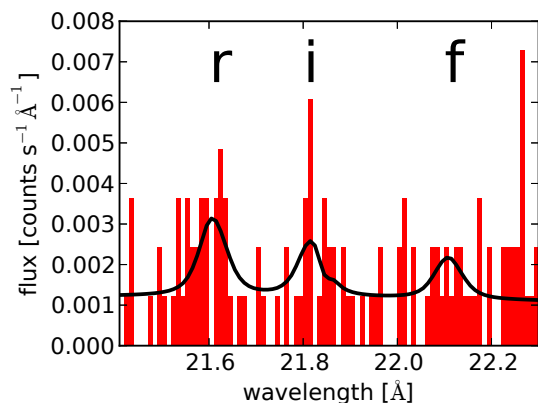


FIG. 4.— O VII He-like triplet with best-fit model. The position of the recombination (*r*), intercombination (*i*) and forbidden (*f*) lines are marked. The best-fit clearly deviates from the low-density regime where  $f/i = 3.8$ .

upper level of the *f* to the *i* line. In MN Lup the UV field is insufficient to influence the *R*-ratio of the observed Ne and O triplets, so any deviation must be caused by the density in the emitting region. The *G*-ratio varies slowly with the plasma temperature. The low count numbers and consequently large uncertainties do not allow us to constrain the temperature meaningfully from this ratio.

Figure 4 shows the O VII triplet. The measured *R*-ratio is 0.75 ( $n_e \approx 2 \times 10^{11} \text{ cm}^{-3}$ ). Due to the low number of counts the errors are non-Gaussian and strongly asymmetric, so we performed Monte-Carlo simulations to estimate the confidence limits. We run 10,000 simulations; in each of them the number of counts in each bin is drawn from a Poisson distribution with the best fit-model as expectation value. We fit the background level and the amplitude of the three lines to the simulated spectra in the same way we treat the observed data. This procedure is very similar to that employed by Günther & Schmitt (2009, appendix A), where more details can be found. According to the CHIANTI spectral database (Dere et al. 1997, 2009) the low-density limit of the O VII *R*-ratio is 3.8. Our Monte-Carlo simulations show that the data exclude the low-density limit ( $n_e \lesssim 10^9 \text{ cm}^{-3}$ ) with 93% significance and give  $1\sigma$  confidence for  $R < 1.16$  ( $n_e > 3 \times 10^{10} \text{ cm}^{-3}$ ), but we cannot place an upper limit on the density.

For Ne IX the measured *R*-ratio is 1.75 ( $n_e \approx 4 \times$

$10^{11} \text{ cm}^{-3}$ ). This triplet, especially the *i* line, can be blended by lines of Fe XVII, Fe XIX and Fe XX. Given the low signal-noise ratio in the data a detailed deblending as in Ness & Jordan (2008) is not possible. Using CHIANTI we find that the strongest blend from Fe XVII is a line at 13.82 Å; however, at its peak formation temperature, the flux in this line is still only 4% of the flux in the Fe XVII lines at 17.05 and 17.10 Å. Thus, its maximum contribution to the Ne IX *f* line is less than 10% of the statistical uncertainty (table 4). To assess the importance of other Fe ionization stages, we simulate spectra using the emission measures in table 3. Even in the flare, when the Fe XIX and Fe XX lines are strongest, Fe XX 13.78 and 13.84 Å, the strongest blends, have a flux of only 12% of the flux in the Fe XVII lines at 17.05 and 17.10 Å. Since the emission measure of the hot plasma outside of the flare is only a fifth of the emission measure during the flare, the average contribution is much less. Thus, these lines also contribute less than 10% of the statistical uncertainty to the Ne IX *f* line. For the temperature observed, the contamination of the Ne IX *r* and *i* lines is even lower. Thus, we can neglect the blends and find that the observed ratio is compatible with the low-density limit ( $n_e \lesssim 3 \times 10^{10} \text{ cm}^{-3}$ ) on the  $1\sigma$  level, but we can exclude densities above  $3 \times 10^{12} \text{ cm}^{-3}$  at the 95% confidence level.

In summary, intermediate densities in the range  $3 \times 10^{10} < n_e < 3 \times 10^{12} \text{ cm}^{-3}$  are compatible with both triplets. In the above discussion it is assumed that all emission seen in a triplet originates in a homogeneous plasma. This is not necessarily the case, as multiple components with different densities could contribute to the observed line fluxes. To estimate the minimum emission measure of the dense component, we consider the most extreme case where the O VII triplet comes from a superposition of a cool corona, which is in the low-density range, and some plasma in the high-density limit. The corona would contribute virtually nothing to the *i* line, but explain most of the *f* line flux, while the converse is true for the dense component. Since both lines are of comparable strength, each component must have about half of the total emission measure for O VII.

#### 4.4. Soft excess

CTTS show an excess of soft plasma compared to main-sequence (MS) stars of similar total luminosity.

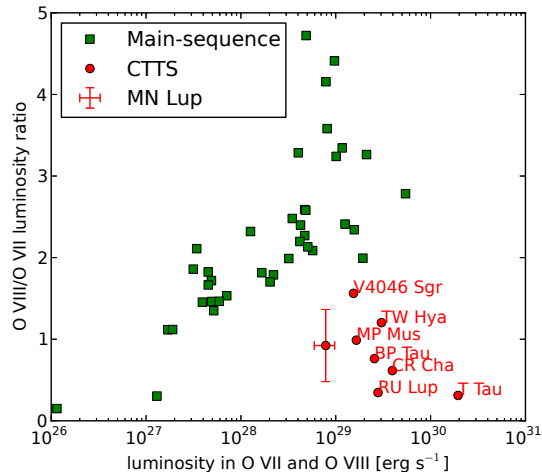


FIG. 5.— The ratio of the O VIII 18.97 Å line and O VII triplet ( $r+i+f$ ) luminosities is a temperature indicator. All CTTS show a soft excess when compared to MS stars of similar total luminosity. See the electronic edition of the Journal for a color version of this figure.

Observationally, a lower ratio of the O VIII/O VII luminosities (Robrade & Schmitt 2007; Güdel & Telleschi 2007) indicates an additional soft emission component around 1-2 MK. As this is only seen in accreting CTTS and Herbig Ae/Be stars (HAeBe), it has to be related to the accretion shock. Figure 5 shows the O VIII/O VII ratio for MS stars from the sample of Ness et al. (2004) and CTTS collected from the literature (references are given in Sect. 1). All fluxes are corrected for absorption using the  $N_H$  values found in a global fit to the X-ray data.

In order to calculate the flux ratio, grating spectroscopy is required. Thus, only bright CTTS with little absorption can be placed on the diagram. The sample of MS stars includes much closer and fainter objects. When compared to MS stars of similar luminosity, CTTS show a soft excess. MN Lup is shown in the figure as a CTTS, based on the fitted model with the lower absorption. It has the lowest total luminosity of all CTTS in the sample. The soft excess is almost certainly related to accretion, although it may not be formed in the post-shock zone. Brickhouse et al. (2010) measure density differences between O VII and Ne IX in the CTTS TW Hya and find that the O VII emission is not compatible with an origin in the post-shock cooling zone according to current shock models (see next section), but can be explained by a lower density corona fed by the accretion stream.

#### 4.5. Shock models

The soft excess and the high densities found in the O VII triplet indicate an accretion shock origin of the soft plasma component. Therefore, we fit the CCD data and the RGS data simultaneously to an accretion shock model. Due to the low count number, the RGS data cannot be binned or the information contained in the He-like triplets would be lost. We use the Cash statistic (Cash 1979) as implemented in Sherpa, which is appropriate for Poisson-distributed low count data. Unlike the  $\chi^2$  statistic, the Cash-statistic does not provide an intrinsic measure of the goodness-of-fit. We replace the coolest component of the three temperature fit in Sect. 4.2 with the accretion shock models of Günther et al. (2007), up-

dated in Günther (2011). Abundances and the absorbing column density are fixed at the values in table 3. We fit the RGS data and the binned EPIC data from 2011. While we use all the RGS data, we restrict the EPIC data to the quiescent phase (before  $t = 98$  ks, see Fig. 1). The background for the EPIC detectors is negligible and we assume a constant background for the RGS, which is not subtracted from the data, but fitted simultaneously to conserve the Poisson counting statistic in the spectrum.

The shock model is described in detail in Günther et al. (2007). The simulations assume a 1-dimensional geometry and an optically thin post-shock cooling zone. The accreting matter is heated in a strong shock and then cools down radiatively. Half of the radiation is directed inwards and absorbed by deeper photospheric layers, the other half of the radiation escapes. The temperature distribution behind the shock is calculated and integrated spectra for different pre-shock densities and velocities are tabulated. The model assumes a Maxwellian distribution for both electron and ions, but it allows for different temperatures in those components, since ions are heated to much higher temperatures in the shock and Coulomb interactions between electrons and ions equilibrate the temperatures only slowly. At each step, the simulation explicitly solves the rate equations for ionization and recombination because these time scales can be longer than the dynamical time scale for some ions, so that the post-shock plasma is not in ionization equilibrium. Thermal conduction is negligible in the post-shock plasma, since the required time scales are much longer than the time it takes for one packet of plasma to travel through the cooling zone. Additionally, heat transport between the post-shock plasma and the surrounding atmosphere is suppressed by the magnetic field of the accretion funnel.

The biggest caveat is that the simulations assume the medium to be optically thin. No line opacity is expected in the X-ray range as calculated a posteriori and this is confirmed by the observed  $r/(f+i)$  ratio in the triplets which matches optically thin predictions; we fit and account for continuum absorption  $N_H$ . However, Drake (2005) argues that (a significant part) of the accretion shock could be buried so deep in the atmosphere, that it is entirely absorbed. In this case, the mass accretion rate that we fit below is to be understood as a lower limit to the total mass accretion rate.

During the fit, the grid of spectra is interpolated in the parameters pre-shock velocity  $v_0$  and density  $n_0$ . Table 5 shows the best-fit parameters of the shock model.

Compared to the fit in Sect. 4.2 the fit statistic improves when one shock model and two single-temperature components (which represent the coronal contribution) are used in the model instead of three single-temperature components. This model reproduces the O VII  $R$ -ratio. The emission measure and the temperature of the hot components change only marginally. The shock component has a pre-shock velocity  $v_0$  of 500 km s $^{-1}$  and a pre-shock density  $n_0$  of  $1.0 \times 10^{10}$  cm $^{-3}$ . The statistical error on the velocity is smaller than the grid step size of 50 km s $^{-1}$ . Given the accuracy of the model grid, we give the model grid step size in table 5 as uncertainty of the fit values. Due to the low count number there is no formal lower limit on the density in the global fit. The normalization of the shock model is directly related to the shock area  $A$ . From these numbers the accretion

TABLE 5  
BEST-FIT MODEL PARAMETERS FOR THE QUIESCENT INTERVAL IN  
2011 ( $1\sigma$  CONFIDENCE INTERVALS).

parameter	model	unit
$N_H$	$=0.21$	$10^{21} \text{cm}^{-2}$
$VEM_1$	$2.0 \pm 0.1$	$10^{52} \text{cm}^{-3}$
$VEM_2$	$2.1 \pm 0.2$	$10^{52} \text{cm}^{-3}$
$kT_1$	$0.77 \pm 0.04$	keV
$kT_2$	$2.4 \pm 0.2$	keV
$v_0$	$510 \pm 50$	$\text{km s}^{-1}$
$n_0$	$1 \pm 1^a$	$10^{10} \text{cm}^{-3}$
$A_{spot}$	$10_{-3}^{+1}$	$10^{20} \text{cm}^2$
$\dot{M}$	$2 \times 10^{-11}$	$M_\odot \text{yr}^{-1}$
$L_{shock}/L_{corona}$	0.46	

<sup>a</sup>More stringent limits can be derived from analysis the He-like triplets alone (see text).

rate  $\dot{M}$  can be calculated as:

$$\dot{M} = \mu m_H n_0 v_0 A, \quad (1)$$

where  $\mu$  is the dimensionless mean particle mass, averaged over electrons and ions and  $m_H$  is the mass of the hydrogen atom. Table 5 gives the mass accretion rate. While the uncertainty on  $n_0$  and  $A$  are large, the uncertainty on the mass accretion rate is much lower, because it is determined from the normalization of the shock model, while the density is only constrained by the  $f/i$  ratio in the He-like triplets. The fitted value for the size of the accretion spot implies a surface filling factor of 2%. As estimated in Sect. 4.3 at most half of the cool plasma can be explained by coronal emission. Thus, the shock luminosity (and consequently the accretion rate) of the shock may be overestimated by a factor of 2 at most. The free-fall velocity from infinity is

$$v_{ff} = \sqrt{\frac{2GM_*}{R_*}} \quad (2)$$

where  $G$  is the gravitational constant. For a stellar radius of  $R_* = 0.87R_\odot$  and a mass of  $M_* = 0.68M_\odot$  (Strassmeier et al. 2005) this leads to a free-fall velocity of  $550 \text{ km s}^{-1}$  in very good agreement with the values derived above.

#### 4.6. Variability in the optical spectrum

The optical spectra of MN Lup are dominated by the Balmer series and Ca II H and K in emission, telluric absorption, and photospheric absorption lines. MN Lup has been Doppler imaged with *VLT/UVES* before by Strassmeier et al. (2005) and we refer to that paper for a figure of the optical spectrum of MN Lup and its general properties. Our data is very similar except for the absence of airglow emission that plagued the analysis in the previous paper. Figure 6 shows the Ca II K, H $\alpha$ , and Li I 6708 Å lines and another absorption line that we identify as Ca I 6103 Å. Strassmeier et al. (2005) suggest this to be the Fe I line at 6102 Å with a blend from an excited Li line at 6104 Å, but the VALD database (Kupka et al. 2000) indicates that the Ca I line is stronger given the effective temperature of MN Lup and assuming solar metallicity. Furthermore, this line identification agrees better with our determined radial velocity of MN Lup than Strassmeier et al.'s identification.

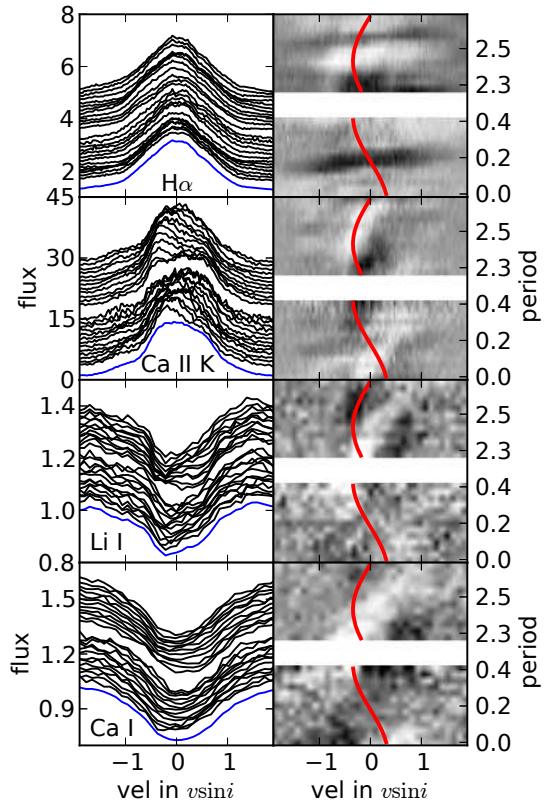


FIG. 6.— Temporal variability of selected lines in MN Lup (Ca II K at 3933.66 Å, H $\alpha$  at 6564.89 Å, Li I at 6707.84 Å, and Ca I at 6102.73 Å). *left*: The spectra are continuum normalized and offset along the y-axis for clarity. Time starts from the bottom and the break between the two nights is not to scale. Due to the lower signal, the absorption lines are binned to a larger bin width than the emission lines. The blue line in each panel shows the mean line profile. *right*: Gray scale representation of the residuals to the mean spectrum. As an example, the red curve shows the position of a tentative spot with  $\theta = 70^\circ$  and phase  $\phi = 0.68$ . Clearly, the line deformations do not follow this red line through all observed phases, see text for discussion.

Variability within a night and between the two nights can be seen in all lines in the figure. All pronounced features move from blue to red through the line profiles which is consistent with rotational modulation. The features in Ca II K, Li I, and Ca I are, at least partially, correlated and their slope in the diagram is very similar. They are most clearly defined between phase 2.3 and 2.7. The second white structure in Ca II K between phase 0.0 and phase 0.2 is less clear.

The modulation features in the H $\alpha$  line profile differ strongly from the other lines in the figure. Possibly, the bright Ca II K feature around phase 2.5 has a broadened counterpart in H $\alpha$ . However, the most prominent variations in H $\alpha$  are the dark features quickly passing through its profile around phases 0.2 and 2.6. We tentatively interpret these dark bands as signatures of co-rotating prominences. Such features are commonly seen on a few highly active fast-rotating stars (most notably AB Dor and BO Mic) (Collier Cameron 1996; Donati et al. 1999; Wolter et al. 2008), but, to our knowledge they have only been found on one other WTTS or CTTS, namely TWA 6 (Skelly et al. 2008). However, the spectral feature ascribed to a prominence in TWA 6 is only seen in emission beyond the stellar disk and not in absorp-



tion above it (see Fig. 16 of Skelly et al. 2008). In our data of MN Lup it is the other way around: We only see the tentative prominences in absorption above the stellar disk. The corresponding features pass from minus to plus  $v \sin i$  in about 0.1 rotations, which corresponds to a height of about two stellar radii above the stellar surface.

Apart from the tentative prominence features, the H $\alpha$  profile variations do not add any information to the following discussion. Thus, we concentrate on Ca II K and the two photospheric lines.

We do not attempt to model the line profiles of MN Lup’s “undisturbed” photosphere or chromosphere – whatever undisturbed could mean in detail in this context. Instead, the gray scale plots in Fig. 6 show the line variations relative to the corresponding mean line profile obtained by averaging all our observed spectra (qualitatively, the gray scale images do not change if a symmetric line profile is used instead of the mean observed profile); dark and light shades indicate less and more flux compared to the mean profile, respectively. In this representation, in general, one can not safely discern an emission feature from an absorption one moving through the line profile. If we interpret the white feature in Ca II K as a chromospheric emission region, then the corresponding dark feature simply results from the normalization. On the other hand, if the dark feature is caused by an absorption feature, then the remaining plot must be brighter simply to fulfill the normalization condition.

Motivated by Strassmeier et al. (2005) finding a potential accretion spot in their Doppler images of MN Lup, we inspected the line profile variations shown in Fig. 6 for signatures of a similar feature. Such as spot should show up as emission, hence bright, feature in the chromospheric emission profiles. On the other hand, it would appear as *dark* feature in most photospheric lines: If the equivalent width of an absorption line is approximately constant or decreases with temperature, then a bright (i.e. hot) spot will cause a *dip* (i.e. depression) in the line profile, because its behavior is dominated by the surrounding quasi-continuum (e.g. Fig. 1 in Vogt & Penrod 1983). The velocity where a rotationally modulated spot at latitude  $\theta$  (defined to be  $90^\circ$  at the pole and  $0^\circ$  at the stellar equator) and longitude  $\phi_0$  ( $\phi_0 = 0$  for spots that pass the center of the stellar disk at phase  $p = 0$ ) is located, can be calculated as

$$v(p) = v \sin(i) \cos(\theta) \sin(2\pi(p - \phi_0)) \quad (3)$$

We did not find any combination of  $\theta$  and  $\phi_0$  that fits slope and visibility of the observed bright feature. As an illustration, the red sinusoidal line in Fig. 6 traces approximately the bright feature in Ca II K between phases 2.3 and 2.7 which could be due to a rotationally modulated hot spot fixed on the stellar surface and rotating with it. In this interpretation, the dark feature around the same phases in Li I, weaker in Ca I, would represent the photospheric signature of the tentative hot accretion spot. However, clearly the red sine does not trace the line profile variations through *all* observed phases: The Ca II K emission feature does not continue before about phase 2.3, and, furthermore, it is not visible two rotations earlier around phase 0.3. The same observation applies to the corresponding dark feature in the Li I line. Thus, the Ca K emission feature does not seem to trace

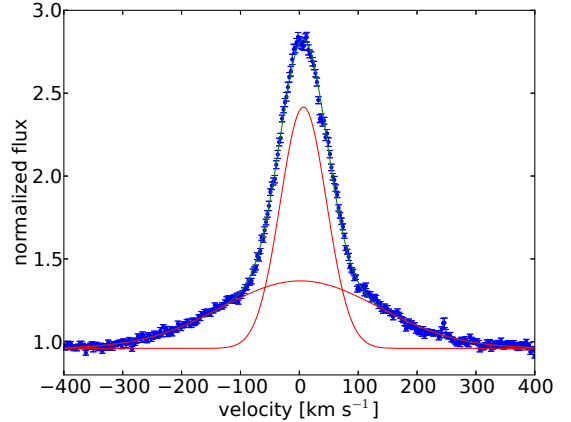


FIG. 7.— Typical H $\alpha$  line profile with a fit of two Gaussian components.

a hot spot on the stellar surface that survives the observed stellar rotations. We come to the same conclusion analyzing the Ca II K emission feature passing the line profile center at about phase 0.1. While the Ca I line shows a fuzzy dark structure at the same phases, this dark structure seems to pass the line profile center at a later phase, not before phase 0.2.

We conclude that the chromospheric and photospheric line profiles in our spectra do not show any clear signature of a hot, i.e. accretion, spot rotating with the stellar surface. On the other hand, our X-ray analysis suggests ongoing weak accretion. Unfortunately, it does not yield any information on the location of this tentative accretion and does not help in the above analysis. If accretion is indeed present, our optical data suggest that the corresponding photospheric and chromospheric signature of the accretion funnel (a) is below our current optical sensitivity, (b) smeared out on the surface or (c) located so close to the visible pole that it does not lead to a significant rotational modulation of the line profile. We cannot exclude any of the above possibilities. However, we consider option (c) rather unlikely because our average line profiles do not show a pronounced deformation near the line center which would be the spectroscopic signature of this scenario.

#### 4.7. The H $\alpha$ line profile

H $\alpha$  and other Balmer lines can be used as an accretion tracer. Figure 1 shows the EW of the H $\alpha$  line together with the X-ray and UV light curves. The time resolution of the UVES data is too low to track the flares seen in the UV, but variability in the H $\alpha$  line exists on longer time scales.

Figure 7 shows a typical H $\alpha$  line profile. The line can be well described by a narrow (FWHM  $\approx 90$  km s $^{-1}$ ) and a wide (FWHM  $\approx 300$  km s $^{-1}$ ) Gaussian component. Both components are almost centered: The narrow component shifts by less than 1 km s $^{-1}$  between the observations, the wide component by 25 km s $^{-1}$ . There are significant differences between the model at +100 and -100 km s $^{-1}$ , indicating that the inner component might differ from a Gaussian in the wings. Strassmeier et al. (2005) found a radial velocity of  $4.4 \pm 2.0$  km s $^{-1}$  and a peak-to-peak variation of the line center of 9 km s $^{-1}$ . The peak-to-peak variation is caused by the wide emission component. Active stars often show H $\alpha$  in emis-

sion with a narrow and symmetric profile (Fang et al. 2009), while accreting CTTS typically show wide and asymmetric profiles with absorption and emission components both on the blue and on the red side of the line due to winds and accretion funnels, respectively. Our observed H $\alpha$  EWs are similar to the value of 6.7 Å found by Krautter et al. (1997).

#### 4.8. Forbidden optical emission lines

We do not see any emission at the position of the [O I] 6364 Å airglow line. A small peak, which is however not significant above the noise, can be found at the [O I] 6300 Å line. Other forbidden emission lines which are commonly found in outflows from CTTS, e.g. [S II] are not visible in the spectrum of Strassmeier et al. (2005) and this is confirmed in our new data. The absence of any outflow tracers is consistent with the simple H $\alpha$  line profile.

### 5. DISCUSSION

#### 5.1. X-ray properties

MN Lup has been observed with *ROSAT* in a survey and in three pointed observations with *XMM-Newton*. MN Lup is no longer embedded in a natal molecular cloud, so the interstellar absorption along the line-of-sight is low, but optical photometry requires reddening towards the stellar photosphere, which, assuming an interstellar  $A_V/N_H$  ratio, predicts an absorbing column density about an order of magnitude larger than observed in our X-ray spectra. We analyze both absorption scenarios in Sect. 4.2 with the result that only the lower absorption column of  $N_H = (2 \pm 1) \times 10^{20} \text{ cm}^{-2}$  leads to physically consistent results.

Assuming a similar absorption, all measured X-ray luminosities from *ROSAT* and *XMM-Newton* agree well. Like the H $\alpha$  emission, the X-ray luminosity does not show a long term trend for the last decade. From the X-ray point of view MN Lup is an active star. Its  $L_X/L_{bol}$  ratio matches that of other saturated TTS or active MS stars.

In all spectra we see evidence of high temperatures, which can only be explained by coronal magnetic activity. Also, there is clear flaring in the lightcurves, both in 2010 and in 2011. In those flares, luminosity and temperature increase as expected for magnetic activity. This finding is supported by the IFIP effect in the elemental abundances, which is common in active stars. Alternatively, this pattern could be due to grain formation, where most of the Fe is bound in grains and remains in the disk, while more volatile gases like Ne remain in the gas phase and are accreted (Stelzer & Schmitt 2004). However, no optically thick dust is observed around MN Lup (see Sect. 5.5)

While the EPIC spectra are all compatible with stellar activity as expected from WTTS or young MS stars, the RGS data exhibit two phenomena, which point towards accretion: The low  $f/i$  ratio in the O VII triplet and the soft excess.

#### 5.2. Mass accretion

Strassmeier et al. (2005) argue that the Doppler image of MN Lup can best be explained, if a part of the photosphere is covered by the accretion funnels. From

their data they cannot determine the mass accretion rate and they adopt  $10^{-9} M_\odot \text{ yr}^{-1}$  as a fiducial value for their magnetic dipole model, which would require a polar magnetic field of 15 kG on the stellar surface. Smaller magnetic fields and accretion rates are possible down to  $10^{-11} M_\odot \text{ yr}^{-1}$ .

Jayawardhana et al. (2003) presented a correlation between accretion and the width of the H $\alpha$  line at 10% of the maximum height. A similar formula was found by White & Basri (2003). There is some discrepancy between the two groups about the borderline between accretion and purely chromospheric activity, as measured by the 10% width of H $\alpha$ . The first article sets this boundary at  $200 \text{ km s}^{-1}$ , the second at  $270 \text{ km s}^{-1}$ . In figure 7 we measure exactly  $270 \text{ km s}^{-1}$ , which would correspond to accretion according to Jayawardhana et al. (2003), while White & Basri (2003) still explain that as chromospheric activity.

Natta et al. (2004) fit a relation between H $\alpha$  line width at 10% of the maximum and the accretion rate for a sample of brown dwarfs accreting at very low rates. While the accretion process could be similar, in the case of MN Lup a much larger fraction of the H $\alpha$  emission is due to chromospheric activity, as the X-ray luminosity proves that it is an active star. Therefore, we consider the value derived from this formula ( $\dot{M} = 5 \times 10^{-11} M_\odot \text{ yr}^{-1}$ ) as an upper limit.

Curran et al. (2011) argue the H $\alpha$  line width at 10% of the maximum to be a good indicator of accretion, but a less reliable way to calculate the accretion rate. Despite this, the upper limit derived above compares well with the accretion rate of  $2 \times 10^{-11} M_\odot \text{ yr}^{-1}$  from our fit of X-ray accretion shock models (Sect. 4.5). This also rules out the scenario where a significant part of the X-ray emission is buried as this would lead to differences between the mass accretion rates measured from H $\alpha$  and X-rays. We conclude that accretion with a very low rate takes place on MN Lup.

One caveat is that the H $\alpha$  line in accreting stars is typically asymmetric (Muzerolle et al. 1998, 2003) because the emission partially originates in the accretion funnels, where we can only observe the red-shifted accretion, since the funnels on the far side of the star are blocked from view. Absorption of the H $\alpha$  emission from the accretion shock or in the chromosphere by a wind or the accretion funnels also leads to asymmetric line profiles. However, for very low accretion rates we expect only weak outflows and weak accretion funnels, thus some geometric configurations could lead to a symmetric H $\alpha$  line profile.

#### 5.3. Rotational modulation

None of the X-ray or UV lightcurves in figure 1 shows any rotational modulation. Specifically, the X-ray lightcurve is flat in 2011 outside the large flare. On the other hand, in the Doppler images of Strassmeier et al. (2005) accretion spots can be seen at almost any rotational phase with changes in the accretion shock area observed and our analysis of the Ca II K, Li I, and Ca I lines shows rotational modulation consistent with a feature at high stellar latitude. While surveys of star forming regions rarely show a correlation between rotationally modulated UV/optical and X-ray lightcurves from CCD data (Stassun et al. 2006; Audard et al. 2007), Argiroffi et al. (2012b) find rotational modulation in V4046 Sgr in

the X-ray grating spectrum by adding up the signal of those lines that are formed predominantly in the accretion shock. The absence of any significant X-ray modulation in the CCD spectra of MN Lup is thus not sufficient to conclude that there is no accretion spot.

#### 5.4. Comparison to other TTS

In many respects MN Lup is similar to IM Lup, a TTS star found in the same star forming region. IM Lup is a transition case between CTTS and WTTS. Its inner disk is already evolved and, similar to MN Lup, the corona shows hot components and an IFIP abundance pattern which point to magnetic activity. Just like MN Lup, the X-ray luminosity of IM Lup is close to the saturation limit (Günther et al. 2010). However, in IM Lup the signal in the grating spectrum is too low to exclude either the high-density or the low-density limit of the  $f/i$  ratio. IM Lup was observed with *Chandra*/HETG which offers a better wavelength resolution, but much lower effective area in the O VII triplet, so the density can only be observed in the Ne IX triplet. Ne IX is formed at a higher temperature, thus it has a stronger coronal contribution and much stronger shocks are required to cause a detectable signal. On the other hand, IM Lup has a more complex H $\alpha$  line with both emission and absorption components. So, both stars seem to show accretion with a very low rate.

In comparison with the sample of CTTS of Günther (2011), which all have X-ray grating spectroscopy, MN Lup shows similar abundances, coronal temperatures and it has a comparable shock speed. However, the density of the accreting plasma is at least an order of magnitude lower than in TW Hya, BP Tau, V4046 Sgr and MP Mus. Surprisingly, due to the much larger area of the accretion spot, the fitted mass accretion rate is similar. This could be partly caused by a selection effect. TTS close to the end of their accretion phase are the best to observe, since the absorption by the cloud is lower than in younger objects. This could cause us to find predominately low, but still detectable, accretion rates. It is possible, that the soft emission in MN Lup is a mixture of a denser accretion shock and a cool corona. In this case the already low mass accretion rate would still be overestimated by a factor of 2 (Sect 4.3).

#### 5.5. Accretion and the absence of a dust disk?

Above, we argued that MN Lup shows some signatures of weak, yet ongoing accretion at a rate of  $2 \times 10^{-11} M_{\odot} \text{ yr}^{-1}$ . However, no IR excess was discovered in the *Spitzer* c2d survey. This sets an upper limit on the fractional disk luminosity of  $L_*/L_d < 9.1 \times 10^{-4}$  (Wahhaj et al. 2010). Obviously, MN Lup does not have a dusty disk, even the debris disk around  $\beta$  Pic has a higher fractional luminosity. How can these two observations be reconciled?

It is instructive to compare MN Lup with CVSO 224, a M4 star with a significantly lower X-ray luminosity ( $\log L_X = 29.3$ , Ingleby et al. 2011), but a few times larger mass accretion rate ( $7 \times 10^{-11} M_{\odot} \text{ yr}^{-1}$ , Espaillat et al. 2008) estimated from a H $\alpha$  line of similar width as in MN Lup, but with a more complex line profile. Espaillat et al. (2008) detect a circumstellar disk with an inner hole of 7 AU that contains small amounts of optically thin dust. In CVSO 224 the observed mass accretion

rate is much lower than the expected photo-evaporation rate given the X-ray and FUV luminosity. Once photoevaporation becomes dominant, the inner disk should clear on a very short time scale. The only way to explain mass accretion in this context is a very massive outer disk that fuels a high accretion rate and due to planets or binary companions only a small fraction of this arrives on the star. Based on this interpretation we postulate an as yet un-observed outer disk for MN Lup. However, the radius of the inner hole needs to be larger than in CVSO 224, since no excess beyond photospheric emission is seen at  $24 \mu\text{m}$  for MN Lup. The c2d survey is most sensitive to micron-sized dust in the inner regions of an accretion disk; only mm data can reveal if a cool outer disk exists. If it does, then it could supply mass at a much higher rate than the observed stellar accretion rate. The inflow would be mostly stopped by photoevaporation as Owen et al. (2012) predict that the X-ray luminosity of MN Lup can drive a photoevaporative wind with a mass loss rate of  $5 \times 10^{-9} M_{\odot} \text{ yr}^{-1}$  – two orders of magnitude higher than the observed stellar mass accretion rate. A second way to explain the mass for the accretion flow without an IR excess are grains so large that they are invisible in the IR. Essentially, the inner disk would consist of sand and gas only. We can even speculate further that these grains may give rise to a secondary debris disk, when stellar activity, and thus the photoevaporation rate, decreases.

Alternatively, the observed phenomenae can be explained by MN Lup’s activity. The H $\alpha$  EW is well within the range of active stars (Worden et al. 1981; Robinson et al. 1990), but the wings of the line are unusually wide. Also, the X-ray luminosity and the IFIP pattern indicate an active star. On the other hand, the low-density limit for the O VII  $f/i$ -ratio is excluded on the 93% confidence level with a lower limit of  $3 \times 10^{10} \text{ cm}^{-3}$ , which is above typical coronal densities in active stars (Testa et al. 2004).

Also, comparing the measured  $N_H$  with the  $A_V$  value from Strassmeier et al. (2005) we find a low  $N_H/A_V$  ratio compared with the ISM. This could be caused by a lower gas-to-dust ratio, though there is no reason to expect that material around MN Lup should be dust-enhanced. On the contrary, the stellar radiation should evaporate the dust. One explanation could be that the reddening is very local. This would fit the suggestions by Strassmeier et al. (2005) that part of the reddening is due to the accretion columns. Conceivably, different X-ray emission components could be effected differently: While the corona is directly observable, the accretion shock might be hidden behind the accretion stream and in X-rays we would measure an average of the different  $N_H$  values. However, the signal-to-noise ratio of the X-ray spectrum is insufficient to fit multiple absorption components. On the other hand, the  $N_H/A_V$  ratio is not only influenced by the gas-to-dust ratio, but also by the dust composition. Grain coagulation can increase the reddening per hydrogen atom and thus cause lower  $N_H/A_V$  ratios. While these changes are most obvious around the silicate feature in the IR, they pertain to optical wavelengths as well (Ormel et al. 2011). Varying  $N_H/A_V$  ratios are observed for different molecular clouds (see e.g. the discussion in Günther et al. 2012), so deviations from the interstellar ratio are certainly consistent

with the presence of circumstellar material.

## 6. SUMMARY AND CONCLUSION

We observed MN Lup with *XMM-Newton* and *VLT/UVES* with some of the data taken simultaneously. There are three short ( $\approx 1$  ks) flares seen in the UV and the X-rays as well as longer periods of enhanced X-ray activity in 2010 and towards the end of the 2011 observations with a harder spectral signature. The short UV and X-ray bursts have all characteristics of solar “white-light” flares.

The X-ray spectrum is fitted with three components, the softest of which is best described by an accretion shock model. The abundances follow an IFIP pattern and the ratio  $L_X/L_{bol} = -2.7$  indicates that MN Lup is an X-ray active star. From the O VII triplet in the grating spectrum we derive a lower limit on the density of  $n_e > 3 \times 10^{10} \text{ cm}^{-3}$ , which is higher than normally seen in active stars on the 93% confidence level. This could be the signature of an accretion shock with a low mass accretion rate around  $2 \times 10^{-11} M_\odot \text{ yr}^{-1}$ . The H $\alpha$  line consists of a narrow and a wide component. While the narrow line is due to chromospheric activity, the wide component again is unusual for active stars on the MS and hints at accretion activity. Analysis of rotationally modulated line profiles in Ca II K, Li I, and Ca I indicates one or more features at high stellar latitude. However, no dust disk that could fuel the accretion was found around MN Lup in a *Spitzer* survey. In the H $\alpha$  line we see a prominence in absorption for the first time in any TTS.

MN Lup is a unique case in the evolution from CTTS to WTTS. While some non-accreting WTTS still retain

detectable disks, MN Lup is the only known case of an accreting star without an IR excess. We propose that MN Lup has lost its optically thick dust only recently. Since photoevaporation clears the inner disk in short time, the continued accretion requires a mass reservoir. No IR excess is detected, so this mass must either be located at large disk radii ( $> 10$  AU) or grain growth has formed an inner disk of particles with sizes of a few mm or above, that do not radiate in the IR. In either case, the disk of MN Lup would be unlike any other known accreting TTS and might well present the very last stage where accretion can be seen. Its radial structure (either a large inner hole or very evolved dust) would be consistent with the recent formation of planetesimals or planets.

It is a lucky coincidence that we could study MN Lup in this detail. Without the archival Doppler imaging, no X-ray observation long enough to measure the  $f/i$  ratio would have been performed and thus it is unlikely that more objects with these characteristics can be found. The next step to test our ideas about the disk of MN Lup is to search for emission from cool dust with mm observations.

Based on observations obtained with *XMM-Newton*, an ESA science mission with instruments and contributions directly funded by ESA Member States and NASA and the ESO VLT. HMG was supported by the National Aeronautics and Space Administration under Grant No. NNX11AD12G issued through the Astrophysics Data Analysis Program.

*Facilities:* XMM VLT:Kueyen

## REFERENCES

- Argiroffi, C., Maggio, A., & Peres, G. 2007, *A&A*, 465, L5  
 Argiroffi, C., et al. 2011, *A&A*, 530, A1  
 —. 2012a, ArXiv e-prints  
 —. 2012b, *ApJ*, 752, 100  
 Audard, M., Briggs, K. R., Grosso, N., Güdel, M., Scelsi, L., Bouvier, J., & Telleschi, A. 2007, *A&A*, 468, 379  
 Baraffe, I., Chabrier, G., Allard, F., & Hauschildt, P. H. 1998, *A&A*, 337, 403  
 Brickhouse, N. S., Cranmer, S. R., Dupree, A. K., Luna, G. J. M., & Wolk, S. 2010, *ApJ*, 710, 1835  
 Brickhouse, N. S., Desai, P., Hoogerwerf, R., Liedahl, D. A., & Smith, R. K. 2005, in *American Institute of Physics Conference Series*, Vol. 774, *X-ray Diagnostics of Astrophysical Plasmas: Theory, Experiment, and Observation*, ed. R. Smith, 405–407  
 Calvet, N., & Gullbring, E. 1998, *ApJ*, 509, 802  
 Cash, W. 1979, *ApJ*, 228, 939  
 Chiang, E., & Murray-Clay, R. 2007, *Nature Physics*, 3, 604  
 Clarke, C. J., Gendrin, A., & Sotomayor, M. 2001, *MNRAS*, 328, 485  
 Collier Cameron, A. 1996, in *IAU Symposium*, Vol. 176, *Stellar Surface Structure*, ed. K. G. Strassmeier & J. L. Linsky, 449  
 Curran, R. L., Argiroffi, C., Sacco, G. G., Orlando, S., Peres, G., Reale, F., & Maggio, A. 2011, *A&A*, 526, A104  
 Dekker, H., D’Odorico, S., Kaufer, A., Delabre, B., & Kotzłowski, H. 2000, in *Society of Photo-Optical Instrumentation Engineers (SPIE) Conference Series*, Vol. 4008, *Society of Photo-Optical Instrumentation Engineers (SPIE) Conference Series*, ed. M. Iye & A. F. Moorwood, 534–545  
 Dere, K. P., Landi, E., Mason, H. E., Monsignori Fossi, B. C., & Young, P. R. 1997, *A&AS*, 125, 149  
 Dere, K. P., Landi, E., Young, P. R., Del Zanna, G., Landini, M., & Mason, H. E. 2009, *A&A*, 498, 915  
 Doe, S., et al. 2007, in *Astronomical Society of the Pacific Conference Series*, Vol. 376, *Astronomical Data Analysis Software and Systems XVI*, ed. R. A. Shaw, F. Hill, & D. J. Bell, 543  
 Donati, J.-F., Collier Cameron, A., Hussain, G. A. J., & Semel, M. 1999, *MNRAS*, 302, 437  
 Drake, J. J. 2005, in *13th Cambridge Workshop on Cool Stars, Stellar Systems and the Sun*, 519–523  
 Espaillat, C., et al. 2008, *ApJ*, 689, L145  
 —. 2010, *ApJ*, 717, 441  
 —. 2012, *ApJ*, 747, 103  
 Fang, M., van Boekel, R., Wang, W., Carmona, A., Sicilia-Aguilar, A., & Henning, T. 2009, *A&A*, 504, 461  
 Feigelson, E. D., & Montmerle, T. 1999, *ARA&A*, 37, 363  
 Fuhrmeister, B., Lalitha, S., Poppenhaeger, K., Rudolf, N., Liefke, C., Reiners, A., Schmitt, J. H. M. M., & Ness, J.-U. 2011, *A&A*, 534, A133  
 Gabriel, A. H., & Jordan, C. 1969, *MNRAS*, 145, 241  
 Gabriel, C., et al. 2004, in *Astronomical Society of the Pacific Conference Series*, Vol. 314, *Astronomical Data Analysis Software and Systems (ADASS) XIII*, ed. F. Ochsenbein, M. G. Allen, & D. Egret, 759+  
 Goldreich, P., & Tremaine, S. 1980, *ApJ*, 241, 425  
 Gorti, U., & Hollenbach, D. 2009, *ApJ*, 690, 1539  
 Grevesse, N., & Sauval, A. J. 1998, *Space Science Reviews*, 85, 161  
 Güdel, M., & Nazé, Y. 2009, *A&A Rev.*, 17, 309  
 Güdel, M., Skinner, S. L., Mel’Nikov, S. Y., Audard, M., Telleschi, A., & Briggs, K. R. 2007, *A&A*, 468, 529  
 Güdel, M., & Telleschi, A. 2007, *A&A*, 474, L25  
 Gullbring, E., Barwig, H., & Schmitt, J. H. M. M. 1997, *A&A*, 324, 155  
 Gullbring, E., Hartmann, L., Briceno, C., & Calvet, N. 1998, *ApJ*, 492, 323  
 Günther, H. M. 2011, *Astronomische Nachrichten*, 332, 448  
 —. 2012, ArXiv e-prints  
 Günther, H. M., Liefke, C., Schmitt, J. H. M. M., Robrade, J., & Ness, J.-U. 2006, *A&A*, 459, L29  
 Günther, H. M., Matt, S. P., Schmitt, J. H. M. M., Güdel, M., Li, Z., & Burton, D. M. 2010, *A&A*, 519, A97+  
 Günther, H. M., & Schmitt, J. H. M. M. 2009, *A&A*, 494, 1041

- Günther, H. M., Schmitt, J. H. M. M., Robrade, J., & Liefke, C. 2007, *A&A*, 466, 1111
- Günther, H. M., et al. 2012, *AJ*, 144, 101
- Huenemoerder, D. P., Kastner, J. H., Testa, P., Schulz, N. S., & Weintraub, D. A. 2007, *ApJ*, 671, 592
- Ingleby, L., Calvet, N., Hernández, J., Briceño, C., Espaillat, C., Miller, J., Bergin, E., & Hartmann, L. 2011, *AJ*, 141, 127
- Jayawardhana, R., Mohanty, S., & Basri, G. 2003, *ApJ*, 592, 282
- Kastner, J. H., Huenemoerder, D. P., Schulz, N. S., Canizares, C. R., & Weintraub, D. A. 2002, *ApJ*, 567, 434
- Koenigl, A. 1991, *ApJ*, 370, L39
- Krautter, J., Wichmann, R., Schmitt, J. H. M. M., Alcalá, J. M., Neuhauser, R., & Terranegra, L. 1997, *A&AS*, 123, 329
- Kupka, F. G., Ryabchikova, T. A., Piskunov, N. E., Stempels, H. C., & Weiss, W. W. 2000, *Baltic Astronomy*, 9, 590
- Littlefair, S. P., Naylor, T., Harries, T. J., Retter, A., & O'Toole, S. 2004, *MNRAS*, 347, 937
- Long, M., Romanova, M. M., & Lamb, F. K. 2012, "New Astronomy", 17, 232
- Muzerolle, J., Calvet, N., & Hartmann, L. 1998, *ApJ*, 492, 743
- Muzerolle, J., Hillenbrand, L., Calvet, N., Briceño, C., & Hartmann, L. 2003, *ApJ*, 592, 266
- Natta, A., Testi, L., Muzerolle, J., Randich, S., Comerón, F., & Persi, P. 2004, *A&A*, 424, 603
- Ness, J.-U., Güdel, M., Schmitt, J. H. M. M., Audard, M., & Telleschi, A. 2004, *A&A*, 427, 667
- Ness, J.-U., & Jordan, C. 2008, *MNRAS*, 385, 1691
- Ormel, C. W., Min, M., Tielens, A. G. G. M., Dominik, C., & Paszun, D. 2011, *A&A*, 532, A43
- Owen, J. E., Clarke, C. J., & Ercolano, B. 2012, *MNRAS*, 422, 1880
- Padgett, D. L., et al. 2006, *ApJ*, 645, 1283
- Petrov, P. P., Gahm, G. F., Stempels, H. C., Walter, F. M., & Artemenko, S. A. 2011, *A&A*, 535, A6
- Porquet, D., Mewe, R., Dubau, J., Raassen, A. J. J., & Kaastra, J. S. 2001, *A&A*, 376, 1113
- Quillen, A. C., Blackman, E. G., Frank, A., & Varnière, P. 2004, *ApJ*, 612, L137
- Raassen, A. J. J. 2009, *A&A*, 505, 755
- Riaz, B., Gizis, J. E., & Harvin, J. 2006, *AJ*, 132, 866
- Rice, W. K. M., Wood, K., Armitage, P. J., Whitney, B. A., & Bjorkman, J. E. 2003, *MNRAS*, 342, 79
- Robinson, R. D., Cram, L. E., & Giampapa, M. S. 1990, *ApJS*, 74, 891
- Robrade, J., & Schmitt, J. H. M. M. 2007, *A&A*, 473, 229
- Schmitt, J. H. M. M., Reale, F., Liefke, C., Wolter, U., Fuhrmeister, B., Reiners, A., & Peres, G. 2008, *A&A*, 481, 799
- Schmitt, J. H. M. M., Robrade, J., Ness, J.-U., Favata, F., & Stelzer, B. 2005, *A&A*, 432, L35
- Shu, F., Najita, J., Ostriker, E., Wilkin, F., Ruden, S., & Lizano, S. 1994, *ApJ*, 429, 781
- Siess, L., Dufour, E., & Forestini, M. 2000, *A&A*, 358, 593
- Skelly, M. B., Unruh, Y. C., Collier Cameron, A., Barnes, J. R., Donati, J.-F., Lawson, W. A., & Carter, B. D. 2008, *MNRAS*, 385, 708
- Stassun, K. G., van den Berg, M., Feigelson, E., & Flaccomio, E. 2006, *ApJ*, 649, 914
- Stauffer, J. R., Caillault, J.-P., Gagne, M., Prosser, C. F., & Hartmann, L. W. 1994, *ApJS*, 91, 625
- Stelzer, B., & Schmitt, J. H. M. M. 2004, *A&A*, 418, 687
- Strassmeier, K. G., Rice, J. B., Ritter, A., Küker, M., Hussain, G. A. J., Hubrig, S., & Shobbrook, R. 2005, *A&A*, 440, 1105
- Strom, K. M., Strom, S. E., Edwards, S., Cabrit, S., & Skrutskie, M. F. 1989, *AJ*, 97, 1451
- Testa, P., Drake, J. J., & Peres, G. 2004, *ApJ*, 617, 508
- Vogt, S. S., & Penrod, G. D. 1983, *PASP*, 95, 565
- Vuong, M. H., Montmerle, T., Grosso, N., Feigelson, E. D., Verstraete, L., & Ozawa, H. 2003, *A&A*, 408, 581
- Wahhaj, Z., et al. 2010, *ApJ*, 724, 835
- White, R. J., & Basri, G. 2003, *ApJ*, 582, 1109
- Wichmann, R., Krautter, J., Covino, E., Alcalá, J. M., Neuhaeuser, R., & Schmitt, J. H. M. M. 1997, *A&A*, 320, 185
- Wolter, U., Robrade, J., Schmitt, J. H. M. M., & Ness, J. U. 2008, *A&A*, 478, L11
- Worden, S. P., Schneeberger, T. J., & Giampapa, M. S. 1981, *ApJS*, 46, 159